ORNL/TM-2025/4070

Feasibility Assessment of Using Electrical Impedance Tomography for Damage Localization in Graphite Microreactor Components

Anant Raj
Brandon Schreiber
Pradeep Ramuhalli
Christian M. Petrie

August 2025

OAK RIDGE National Laboratory

ORNL IS MANAGED BY UT-BATTELLE LLC FOR THE US DEPARTMENT OF ENERGY

ORNL/TM-2025/4070

Nuclear Energy and Fuel Cycle Division

FEASIBILITY ASSESSMENT OF USING ELECTRICAL IMPEDANCE TOMOGRAPHY FOR DAMAGE LOCALIZATION IN GRAPHITE MICROREACTOR COMPONENTS

Anant Raj
Brandon Schreiber
Pradeep Ramuhalli
Christian M. Petrie

August 2025

Prepared by
OAK RIDGE NATIONAL LABORATORY
Oak Ridge, TN 37831
managed by
UT-BATTELLE LLC
for the
US DEPARTMENT OF ENERGY
under contract DE-AC05-00OR22725

CONTENTS

LIST OF FIGURES

LIST OF TABLES

ACKNOWLEDGMENTS

This work is supported by the Microreactor Program of the US Department of Energy's Office of Nuclear Energy. Holly Trellue of Los Alamos National Laboratory provided the geometry for the hex block that was used for modeling and experimental testing. Hongbin Sun assisted with setting up a multiplexer for analyzing measurements from multiple electrodes. David Bryant fabricated the hex block samples used for experimental testing. Dan Sweeney helped with conceptualization based on similar work on a different material system.

ABBREVIATIONS

EDM	electric discharge machine
EIT	electrical impedance tomography
LWR	light-water reactor
ML	machine learning

ABSTRACT

Microreactors have great potential to decrease capital costs and construction timelines, reducing the barriers to implementing advanced nuclear reactor technologies. However, the lower power output of these microreactors introduces economic challenges if the operation and maintenance costs cannot be reduced sufficiently. Many microreactor concepts use graphite materials for in-core moderator and structural purposes, which will require periodic inspection or, ideally, in situ structural health monitoring. This work describes an initial evaluation of the feasibility of leveraging graphite's semiconducting properties to perform electrical impedance tomography (EIT) for defect localization.

First, a study was performed to identify the best methods for bonding electrical contacts to minimize the effects of contact resistance that interfere with impedance measurements of the graphite. After determining the best bonding approach, electrodes were attached to multiple graphite components with varying geometries (e.g., simple block and more representative microreactor hexagonal block). In parallel, finite element analysis approaches were developed and implemented to analyze the impact of defects and contact resistances and to inform an iterative inverse model for reconstructing the conductivity distribution.

The results of this study show that defect localization in graphite components is possible using EIT if a sufficient number of electrodes (to improve spatial resolution) can be bonded using a technique with very low contact resistance and those contact resistances remain stable during reactor operation. If the reactor core and vessel design do not allow electrodes to be bonded during reactor operation, then it may be possible to detach/reattach electrodes between reactor operation and outages if a suitable mechanical connection that offers repeatable contact resistance can be identified. Alternatively, future work could focus on identifying contacts that can survive the harsh reactor operating environment so that contacts do not need to be removed.

1. INTRODUCTION

Microreactors offer many benefits compared with conventional gigawatt-scale light-water reactors (LWRs), including factory assembly, transportability, reduced onsite construction, and enhanced passive safety. They are particularly attractive for remote locations, rural communities, military bases, and some industrial sectors, among other applications [1-3]. However, their reduced power output does not offer the same economies of scale, and microreactors would likely require lower operation and maintenance costs compared with those of LWRs to remain economically viable [3]. The US Department of Energy's Office of Nuclear Energy has been funding efforts across multiple programs and national laboratories [4-6] to enhance reactor control automation to reduce the number of operators and thereby a portion of the operation and maintenance costs. However, even if these efforts are successful, automation and enhanced monitoring of other reactor operations will be required to further reduce costs.

Structural health monitoring of microreactors is a particular concern. These reactors will be quite different from conventional LWRs, so they will not have the decades of operational experience to draw upon. Microreactors generally operate at higher temperatures, and many concepts are attempting to reduce the frequency of refueling outages to further improve economics. This will place a larger burden on structural components, pumps, turbines, valves, and heat exchangers to operate longer and under harsher environmental conditions. In addition, the smaller size of microreactors requires some of these components to be located closer to the core, resulting in exposure to higher temperatures and higher levels of radiation (smaller cores have higher radiation leakage). Finally, the more compact reactor size could also make access to some components more difficult.

Longer refueling outages and a more compact core will also introduce challenges for inspecting in-core components. Graphite is one of the most common in-core materials in microreactors that could be exposed to the harshest environmental conditions (outside of the fuel). Graphite is an excellent neutron moderator, and its high-temperature capabilities make it a common choice for some structural applications. Graphite is currently the material of choice for the core block of heat pipe-based microreactors due to its combination of favorable neutronic, structural, and heat transfer properties [7, 8]. However, graphite is known to undergo significant radiation-induced dimensional changes (compaction followed by swelling late in life), creep, and ultimately fracture [9, 10]. Localized cracks or other defects in graphite could prevent heat transfer from the fuel to some of the heat pipes, requiring the surrounding heat pipes to reject even more heat. Previous reports have documented concerns that this could cause cascading failures if the heat pipes cannot handle the excess heat rejection [11]. Therefore, there is increasing interest in the ability to monitor the structural health of graphite components. Ideally this could be done in situ during reactor operation to identify early signs of impending failures and allow the reactor to be safely shut down so that the graphite could be replaced. However, developing sensor technologies that can survive the harsh in-core operating environment may be challenging. Alternatively, techniques that could be deployed during outages to rapidly identify not only signs of failure in graphite components but also the locations of those failures or defects would be of interest.

2. SCOPE OF WORK

The goal of this project is to develop a nondestructive method for evaluating and localizing defects in graphite microreactor components. More specifically, this project evaluates the feasibility of leveraging graphite's semiconducting properties to use electrical impedance tomography (EIT) to identify regions with significant changes in electrical impedance that can be related to specific defects. The first step is to evaluate methods for attaching an array of electrodes throughout the component and to accurately measure electrical impedances across all pairs of electrodes and how they evolve over time. The next step is to develop a computational approach to solve the inverse problem (i.e., estimating the electrical conductivity changes in the graphite using the measurements obtained in the initial step). The long-term goal would be to combine the experimental measurements and computational modeling to determine whether the models, with input from EIT measurements, can locate specific defects in graphite components.

3. METHODOLOGY

3.1 EXPERIMENTAL

3.1.1 Articles Under Test

3.1.1.1 Material

The material under test in these experiments is POCO graphite, which has long been considered for nuclear reactor applications [12] due to its isotropic properties, fine grain structure, and high strength. Because its electrical properties are consistent in all directions, POCO graphite minimizes potential variations in impedance measurements that could otherwise arise from directional anisotropy. These qualities will benefit the sensitivity and reliability of EIT methods for defect detection because any localized impedance changes can be more confidently attributed to anomalies (e.g., cracks, voids, and holes) rather than inherent material property variations in an otherwise defect-free component.

The grade of POCO graphite used in these experiments is AXF-5Q, purchased from POCO Graphite Inc. Notable manufacturer-reported mechanical and electrical properties for EIT measurement can be seen in Table 1.

Table 1. Notable grade AXF-5Q graphite electrical and mechanical properties for EIT measurement [11].

AXF-5Q PROPERTIES	
Electrical Resistivity	1,470 μΩ·cm
Particle Size	5 microns
Pore Size	0.8 microns
Total Porosity	20% volume
Open Porosity	80% of total
Apparent Density	1.78 g/cc

3.1.1.2 Geometry

As shown in Figure 1, initial experimental testing was performed on a rectangular graphite block with the following dimensions: width = 27 mm, length = 111 mm, height = 15 mm. This simple geometry was selected due to ease of fabrication and fixturing design.

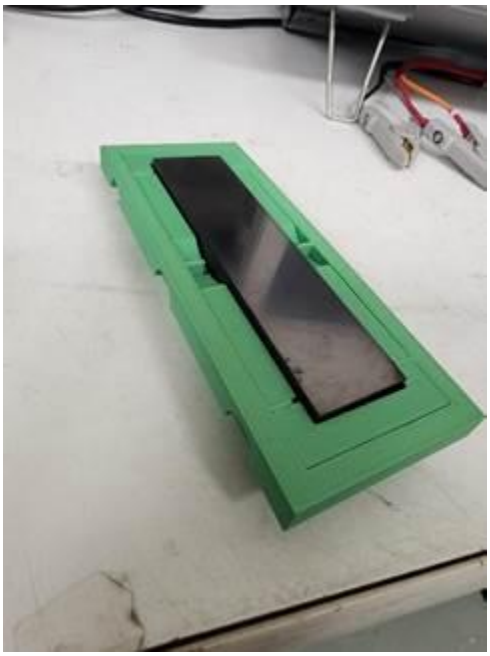

Figure 1. Rectangular graphite sample

After initial testing of the rectangular specimen was complete, researchers fabricated a hexagonal graphite sample for use in later testing to better represent a graphite hexagonal block with heat pipe through holes for use in microreactors. A picture of the sample is shown in Figure 2.

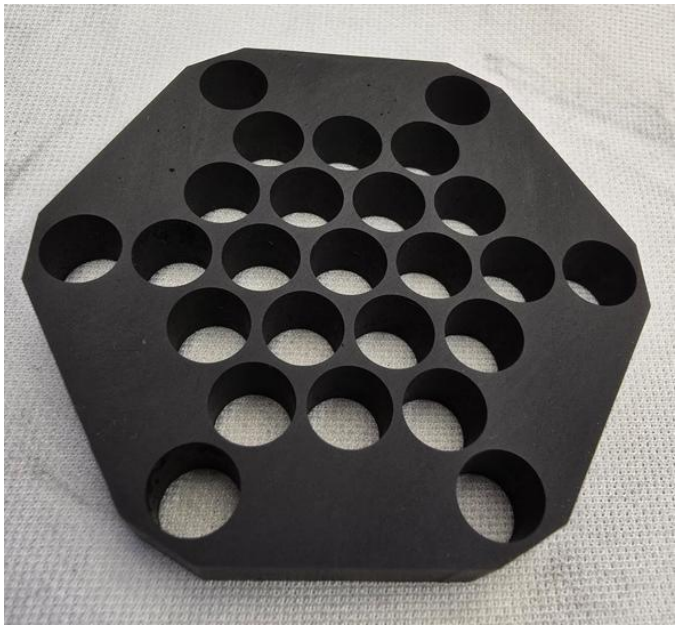

Figure 2. Hexagonal graphite sample.

3.1.2 Electrode Contact Techniques Employed

3.1.2.1 Spring-Loaded Pogo Pins

The first method of making electrical contact with the graphite sample's surface was gold-plated, spring-loaded pogo pins (Figure 3). Spring-loaded pins from Mill-Max (#0914-3-15-20-77-14-11-0) were selected to promote firm contact with the graphite sample's surface regardless of uneven dimensions. This contact method would also have the benefit of being removable from the system and would not require physical modification of the graphite material via drilling or adhesives.

These pins were mounted in a 3D printed fixture to fit snugly around the graphite block (Figure 4). The fixture consisted of three parts: two halves of a surrounding shell that each contained three spring-loaded pins and a third piece that acted as a retaining ring to ensure the pins were at approximately mid-stroke when touching the graphite sample, applying 60 gf (approximately 0.6 N) of pressure at mid-stroke [11].

Figure 3. (a) Single spring-loaded pin located in fixture shell and (b) single spring-loaded pin location on graphite sample surface (with retaining ring removed).

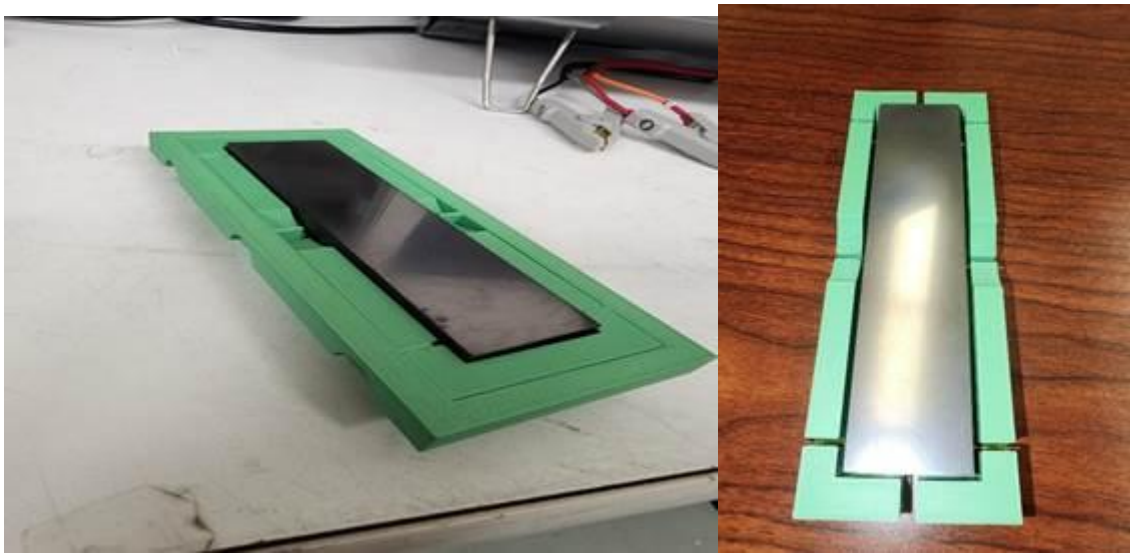

Figure 4. Full fixture installed (a) with retaining ring and (b) without retaining ring.

3.1.2.2 Threaded Contacts (metal posts and graphite electric discharge machine rods)

One route considered for electrically contacting the graphite sample's surface was using threaded posts mechanically coupled into the sample via drilled and tapped holes along the sample's sides. There were concerns that solid metals employed in standard bolts such as steel may fail to achieve proper electrical contact with graphite due to the brittle nature of graphite, which can chip or powder, compromising the connection interface. Dimensional changes in graphite under irradiation could also present challenges for

this mechanical coupling method. Therefore, metal posts were not employed in this feasibility study but may be required in further exploration to verify whether these concerns are valid.

To mitigate this concern, graphite electric discharge machine (EDM) electrode rods were selected as a possible alternative with the thought that a similar material would lessen physical damage or potentially fill in any created voids with more graphite from the rod. However, it was discovered that graphite EDM electrode rods, while conceptually promising, are often not manufactured to standard thread sizes. The specified thread dimensions refer to the hole that the EDM process will produce, not the electrode itself, resulting in mismatch issues. Matching actual physical dimensions to standardized threads could mitigate this issue but requires further exploration.

3.1.2.3 Epoxied Copper Wire

One set of electrodes used in these experiments was standard 22 AWG tinned copper wire adhered to the graphite sample's surface using TIGA 920-H conductive silver epoxy (McMaster-Carr #7661A13), as shown in Figure 5. Before conducting measurements using these epoxied electrodes, the epoxy was allowed to cure for 24 h to ensure mechanical and electrical property stability.

Figure 5. Copper wire adhered to graphite surface with silver epoxy.

3.1.2.4 Tapes (copper foil and conductive fabric)

Two electrically conductive tapes were selected as potential electrodes for testing. A copper foil tape (McMaster-Carr #76555A711) and a conductive fabric tape (McMaster-Carr #3413A41) were adhered to the graphite sample's surface using the tape's included adhesive backing (Figure 6).

Figure 6. (left) Copper tape and (right) conductive fabric tape adhered to the surface of the graphite sample.

After the initial round of testing with the tape's adhesive backing acting as the sole method of contact, another round of testing was performed using the conductive silver epoxy to adhere these materials to the graphite because the epoxy exhibited desirable electrical properties when tested with standard wire. Notably, the epoxy application to the tape electrodes of this first sample was difficult to perform smoothly. Epoxy was applied to the graphite surface, tape was placed on the wet epoxy, and another layer of epoxy was applied to the top of the tape (Figure 7). This application process was perfected in subsequent samples and is discussed later in this report. It is acknowledged that the epoxies used here likely are not suitable for in-core applications and that further development of bonding techniques would be required for such an application.

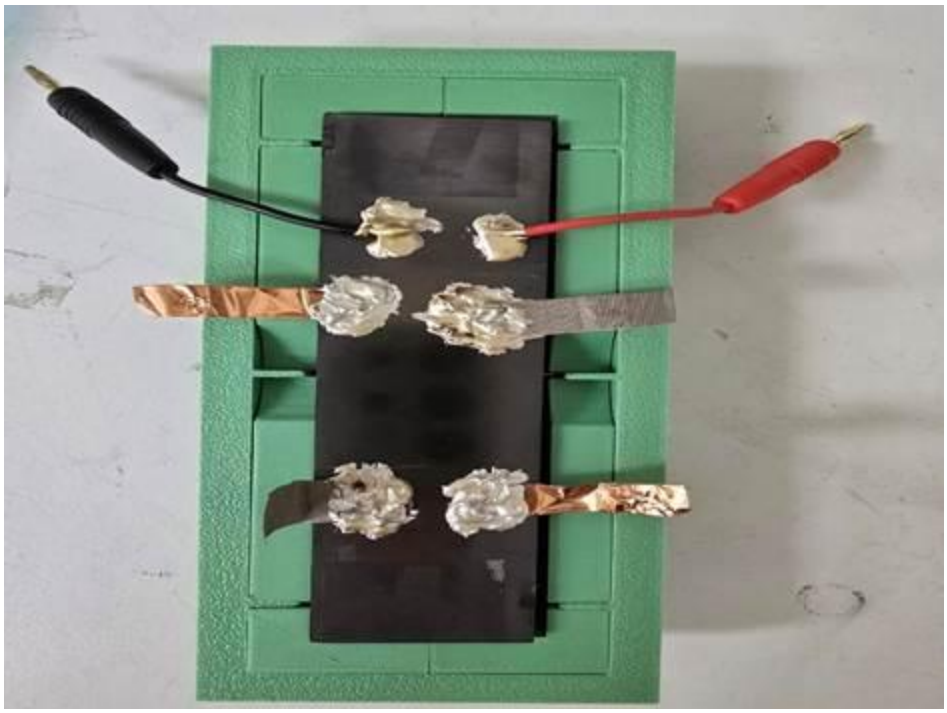

Figure 7. Electrode layout with epoxy used for adhesion at all points.

3.1.3 Equipment

3.1.3.1 Keysight E4990A Impedance Analyzer (20 Hz-20MHz)

This first run of feasibility testing was carried out using a Keysight impedance analyzer (Figure 8). This analyzer allows precise measurement (0.045% accuracy) [12] of impedance across a broad frequency spectrum of 20 Hz–20 MHz. For this testing, a driving voltage of 500 mV was employed, and measurements of electrical properties were taken at 20 Hz, 1 Hz, and 10 kHz frequencies.

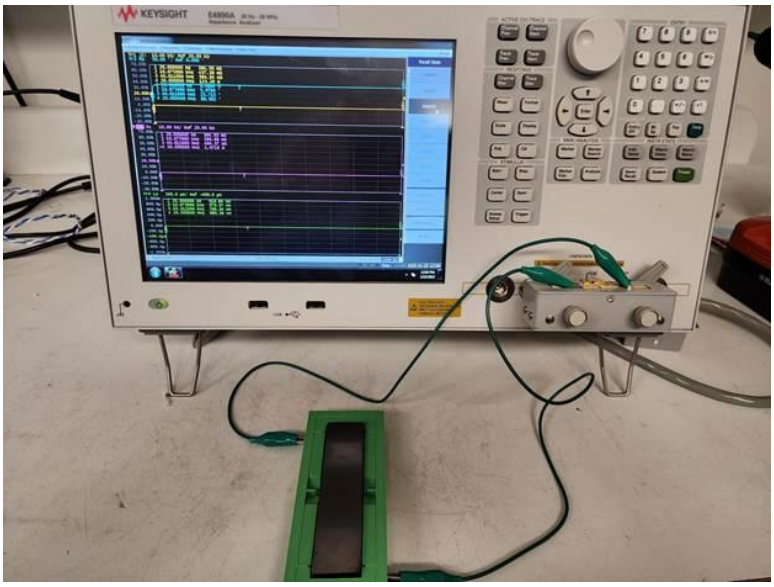

Figure 8. Keysight E4990A impedance analyzer connected to the graphite sample.

3.1.4 Challenges

3.1.4.1 Equipment Resolution/Accuracy

Standard lab multimeters lack the resolution required to measure the sub-ohm resistance values that are observed for contact resistance when comparing electrodes or the sub-ohm resistance across the graphite samples themselves. Equipment such as the aforementioned Keysight E4990A impedance analyzer must be used to obtain precise measurements. This equipment allows for calibration and measurement of values that are accurate to within 0.01 mΩ, enabling comparisons of different electrode pairs that would otherwise be read as nearly (or exactly) the same value in a lower-resolution device.

3.1.4.2 Minimizing Contact Resistance

For EIT measurements, it is critical to ensure that contact resistance remains substantially lower than the intrinsic resistance changes expected from defects; otherwise, measurement accuracy and defect sensitivity are compromised. Electrical contact resistance typically ranges from microohms to milliohms (or higher for poor connections) and can introduce significant errors if not controlled. A method for controlling issues arising from contact resistance is discussed in Section 3.2.

3.1.4.3 Measurement Repeatability

Repeated reconnection of copper tape using alligator clamps leads to deformation and variability in contact resistance, compromising measurement consistency (Figure 9).

Figure 9. Physical deformation of a copper tape electrode.

Even for mechanically stable electrodes, detaching and reattaching electrodes introduces a measurable fluctuation in contact resistance. Future testing will incorporate a multiplexer module such as DAQM903A (Figure 10) to streamline measurements and reduce physical manipulation, improving repeatability. This experimentation intended to include multiplexing testing, but multiple issues with the

control method and calibration issues encountered when using a new potentiostat (Gamry Interface 1010E) delayed this testing until after the writing of this report. Wiring of the control system is complete, and once the new potentiostat is obtaining readings, data can be obtained using this setup to eliminate contact resistance variation.

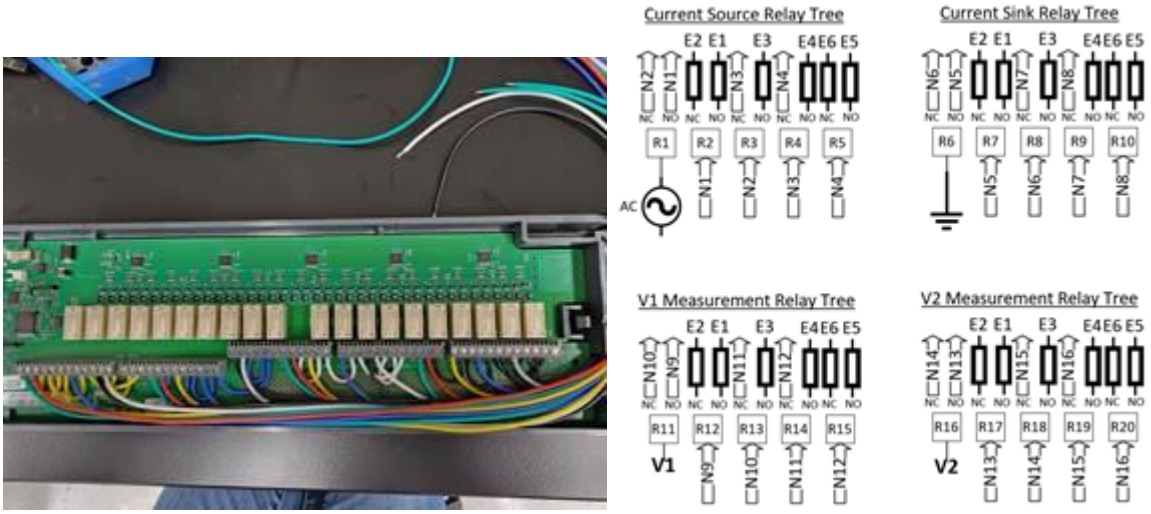

Figure 10. (a) Multiplexer card wired into one of six electrode relay configuration and (b) the relay tree diagram used for wiring.

3.2 MODELING

The standard approach to EIT [13,14] involves connecting multiple electrodes to the sample of interest and applying a current excitation across pairs of electrodes while measuring the voltage at each electrode. The voltage measurements are then used to reconstruct the conductivity distribution across the sample. In this study, an iterative algorithm was employed to perform this reconstruction in a difference EIT setting [13], which entails measuring the potential of each electrode relative to that of a reference electrode. The algorithm involves two key components: (1) a forward model that generates potential field in response to a given current excitation and conductivity distribution and (2) an inverse model that computes the updates to the estimated conductivity based on the difference between the measured and predicted potential response.

3.2.1 Forward Model:

The forward model involves the solution to the conductivity equation as given by [14]:

$$\nabla.\left(\sigma(\boldsymbol{r})\nabla\varphi\left(\sigma(\boldsymbol{r})\right)\right) = 0 \; in \; \Omega \tag{1}$$

where φ is the potential field in response to the conductivity distribution $\sigma(\boldsymbol{r})$ across the sample in the volume Ω due to an applied current excitation at the electrodes given by the boundary condition:

$$\int_{E_l} \sigma \frac{\partial \varphi}{\partial n} ds = I_l \; on \; \partial\Omega \tag{2}$$

Eqn. (2) represents a surface integral along the normal to the boundary $\partial\Omega$ on the l^{th} electrode, and I_l represents the corresponding current excitation.

In the present study, we use Ansys Maxwell [15] to solve the equation (number) for an AC current excitation between electrodes at 60 Hz. For exciting a pair of electrodes, *m* and *n*, we set a 1 A current excitation at the face of electrode *m*, and electrode *n* is set as sink.

Two sample geometries were evaluated. Figure 11 shows the first sample, represented by a thin rectangular graphite block (shown in grey). This sample was selected because of its simplicity, making it amicable for setting up the initial model framework and experimental tests. Six brass electrodes were attached to the side walls (shown in green), consistent with the initial experimental setup.

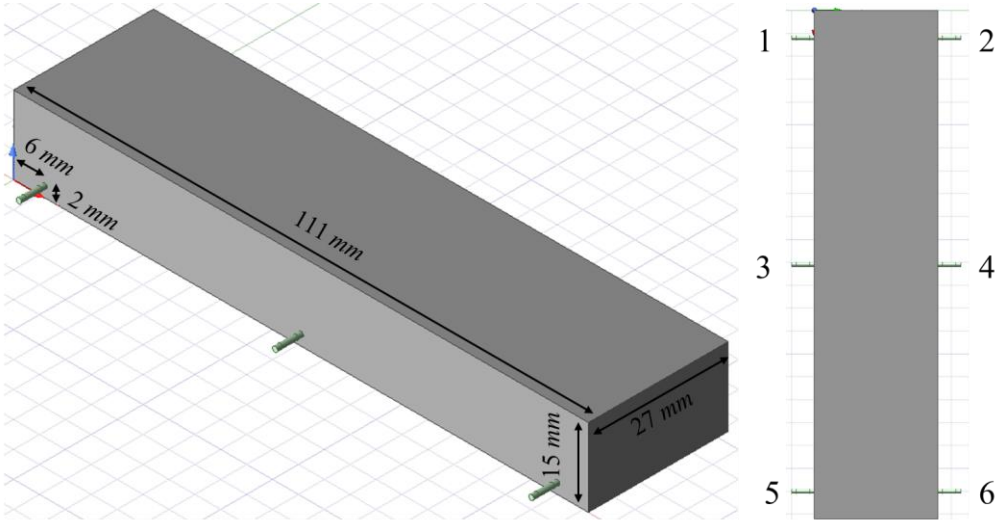

Figure 11. Thin rectangular graphite block with six electrodes attached to the side walls.

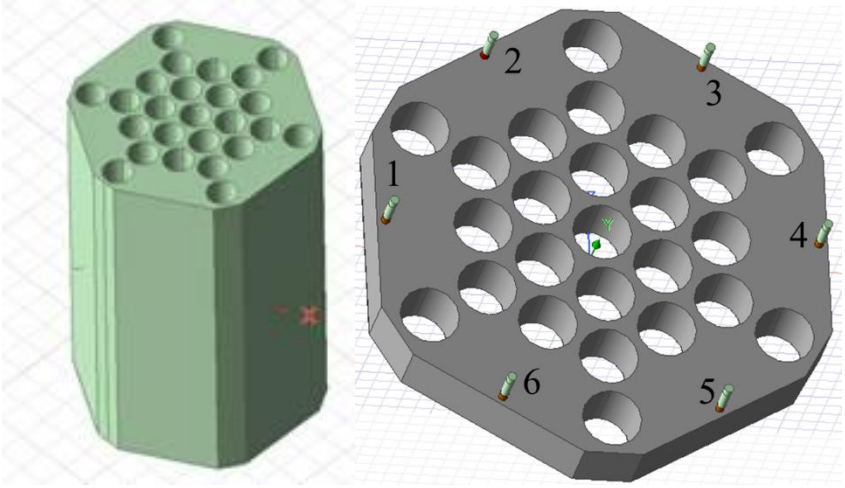

Figure 12. (left) Hexagonal graphite block, representative of the graphite core, and (right) a thin slice of the hexagonal block with six electrodes, scaled down (1:3) for ease of experimentation and faster simulations.

The left panel of Figure 12 shows the second sample that consists of a hexagonal block graphite, which is representative of the graphite core in microreactors. The first set of simulations were performed on this sample for qualitative analysis. Later, the sample was scaled down by a factor of 3.0, and a thin slice was cut out for ease of experimentation and faster simulations. Six brass electrodes (shown in green) were attached to the top face. The scaled sample is shown in the right panel of Figure 12.

For both samples, the graphite and brass properties were obtained from the Ansys materials library; in particular, the conductivity for the two materials was set as 70,000 and 15,000,000 S/m, respectively. Note that there is a wide range for the estimated value of conductivity for graphite (10,000 to 100,000). The 70,000 S/m value is consistent with the manufacturer's estimate for nominal bulk conductivity of POCO graphite; the actual conductivity of a given sample can vary. The conductivity value in the simulations was later scaled to show better agreement with the experimental measurements of the tested samples. More details can be found in the next section.

The initial experiments on Sample 1 indicated challenges with repeatability in resistance measurements caused by variations in contact resistance in the setup shown in Figure 13. To overcome these challenges, copper wire electrodes were connected to the top face of the sample using silver epoxy, which resulted in better repeatability. The top face connection was not updated in the simulations for Sample 1 but was incorporated in Sample 2, as shown previously. The contact resistance was incorporated into both samples using the setup shown in Figure 13. A close-up of the updated electrode is shown in the left panel. The thin, cylindrical electrode was divided into three sections that were 1, 3, and 1 mm in length. The first two sections were modeled using brass and are shown in green. The voltage measurement in the simulations was approximated as the mean voltage on the outer 1 mm section. The current excitations were applied to the outer face of this section. The conductivity of the inner 1 mm section shown in brown was controlled to incorporate contact resistances ($R = \frac{h}{\sigma \pi r^2}$) consistent with the experiments. Consider measuring the resistance between electrodes 1 and 3, as shown in the right panel of Figure 13. The total resistance between the electrodes can be approximated as the sum of the resistance between the points in the sample where electrodes 1 and 3 connect to the sample, plus the contact resistance at electrodes 1 and 3. In general, for electrodes pair *m*, *n*:

$$R_{mn}^{Total} = R_m^{Contact} + R_{mn} + R_n^{Contact} \tag{3}$$

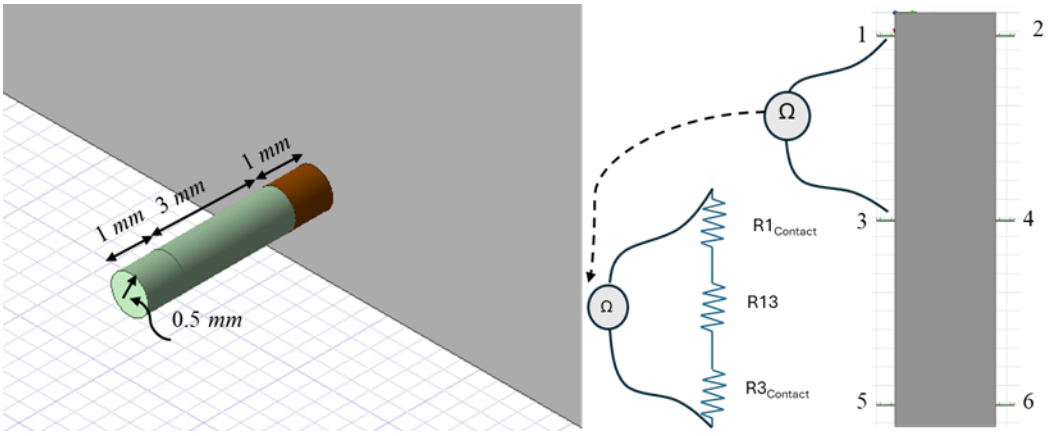

Figure 13. Approach for contact resistance. (left) Electrodes modeled as thin cylinders: the first two parts shown in green are modeled with brass, and the conductivity of the third part shown in brown is controlled to model the contact resistance variations. (right) The resistance between electrodes 1 and 3 is approximated as the sum of sample resistance and contact resistance.

The electrode is connected to the measurement device via wires, and these connections also impart some varying resistance. The net contact resistance is the sum of these and the resistance at the contact of the electrode and the sample:

$$R_m^{Contact} = R_m^{Contact\ at\ sample} + R_m^{Contact\ at\ wire} \tag{4}$$

The two components of the contact resistance in Eqn. (4) can be approximated as samples from a Gaussian distribution whose mean and standard deviation are fixed by the electrode material, sample material, connecting agent, and connecting wires. Thus:

$$R_m^{Contact\ at\ sample} = \langle R^{Contact\ at\ sample} \rangle + \delta R_m^{Contact\ at\ sample} \quad (5)$$

$$R_m^{Contact\ at\ wire} = \langle R^{Contact\ at\ wire} \rangle + \delta R_m^{Contact\ at\ wire} \quad (6)$$

The <> brackets in Eqns. (5) and (6) represent the mean expectation value, which is independent of electrode m, and δ represents the deviation, which is m dependent. The total variance in contact resistance is thus the sum of variances from contact at sample and contact at wire. It is assumed that the value of the resistance for the contact at the sample gets fixed once the electrodes are attached to the sample using the silver epoxy. The value of the resistance due to contact at the wire will vary every time the sample is connected to the measurement apparatus. The conductivity of the third section (shown in brown) in Figure 13 is controlled to incorporate the impact of both of these factors. Note that the first two sections in the electrode impart a small resistance of 0.34 mΩ, which is subtracted to match the overall resistance.

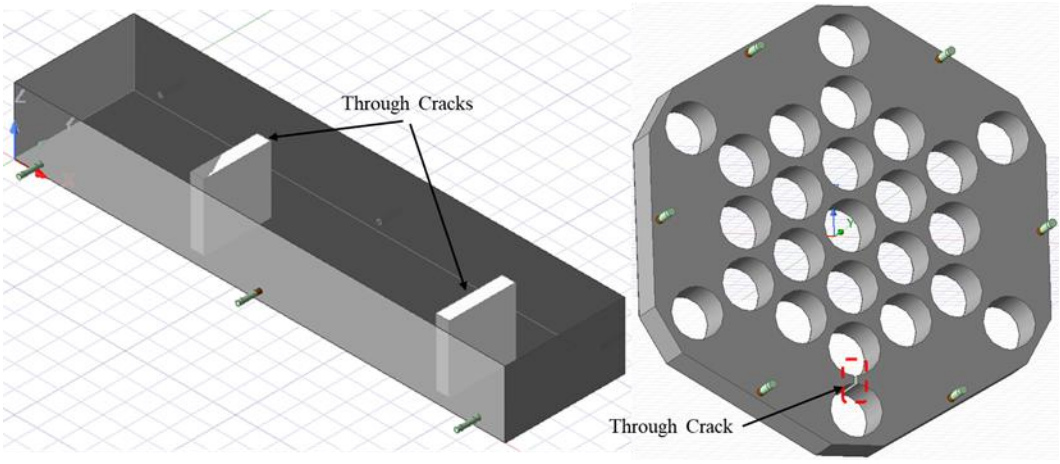

Figure 14. Example of representative defects: (left) two through cracks in the rectangular sample and (right) a thin, through crack between two slots (marked with dashed red box) in the hexagonal block sample.

Defects were incorporated into the sample as through cracks. The left panel of Figure 14 shows two through cracks in the rectangular samples, and the right panel shows a small crack between two cylindrical slots in the hexagonal sample, marked by a dashed red box. The objective is to quantify the change in impedance and resulting voltage drop caused by these defects and to test if the inverse model can detect and localize the defects as regions of low conductivity in the reconstructed images.

3.2.2 Inverse Model

Figure 15 depicts the overview of the inverse model. The inverse model involves reconstructing the conductivity distribution using the voltage measurements from each electrode pair excitation. The team adopted a difference EIT approach [13,14,16] for this study. Consider a 1 A current excitation on electrode m, and electrode n is set as the sink. The voltage at all electrodes is measured with respect to n. For a six-electrode setup, this gives a vector of length 5. For example, the voltage vector for excitation pair 1, 2, where electrode 2 is set as the sink and is given in the following:

$$\boldsymbol{V}_{12} = \begin{pmatrix} V_{12}^{12} \\ V_{32}^{12} \\ V_{42}^{12} \\ V_{52}^{12} \\ V_{62}^{12} \end{pmatrix} \tag{7}$$

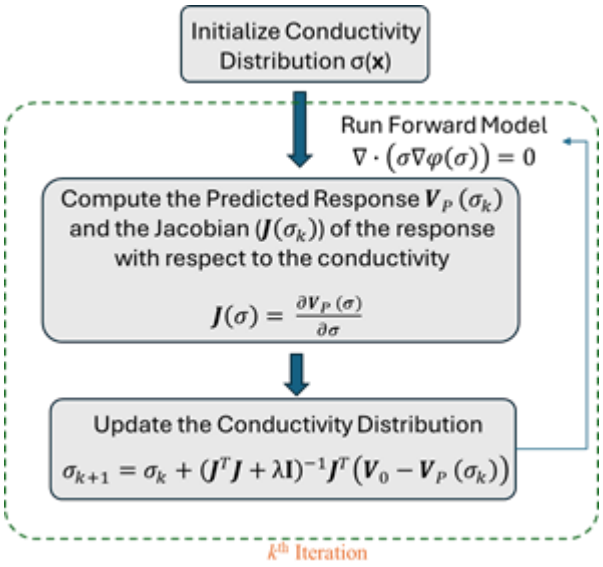

Figure 15. Overview of the iterative algorithm for the inverse model of EIT.

The term V_{pn}^{mn} is the potential difference between electrodes p and n when a current is applied across electrodes m and n (n being the sink).

All possible pairs are excited sequentially, resulting in 15 unique excitations for a six-electrode system. The voltage vectors from all of these are stacked into one 75 × 1 vector:

$$\boldsymbol{V} = \begin{pmatrix} \boldsymbol{V}_{12} \\ \boldsymbol{V}_{13} \\ \vdots \\ \boldsymbol{V}_{56} \end{pmatrix}_{75\times 1} \tag{8}$$

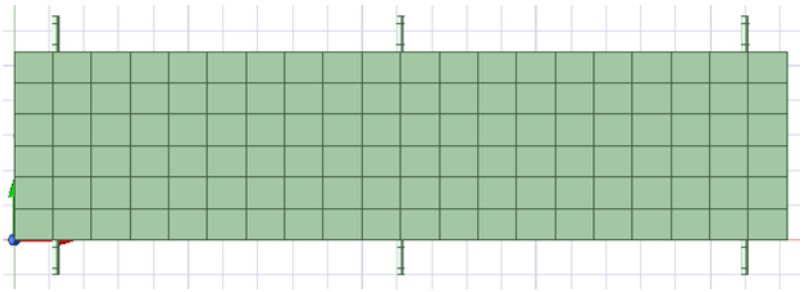

Figure 16. Discretization of the sample domain into a grid for reconstructing the conductivity distribution.

The algorithm starts with getting the voltage measurement vector, V (as shown in Eqn. [7]), for the sample of interest. This is the reference measurement, called $\boldsymbol{V}_0$. Next, the sample domain for the simulations is discretized into a Cartesian grid, as shown in Figure 16. (A grid size of 20 × 6 was selected

for this initial study.) The conductivity for each cell in the grid is initialized to a constant value equal to the conductivity of graphite. The forward model is simulated to obtain the predicted value of the voltage vector, called $\boldsymbol{V}_P$. Further, the forward model is used to compute the Jacobian matrix, which is the sensitivity of the voltage response to the conductivity of each cell in the grid:

$$\boldsymbol{J}\big(\sigma(\boldsymbol{r})\big) = \frac{\partial \boldsymbol{V}_P}{\partial \sigma} \tag{9}$$

$$J_i^{mn\to pn}\big(\sigma(\boldsymbol{r})\big) = \frac{\partial V_{pn}^{mn}}{\partial \sigma_i} \tag{10}$$

Eqn. (9) describes the sensitivity of the voltage difference between electrodes *p* and *n*, due to the conductivity of the i^{th} cell, when a current is applied across the electrodes *m* and *n*. The brute force approach to obtaining the matrix described previously is to perturb the conductivity of each cell by a small amount and run the forward model while holding all the other cells constant. However, this is computationally too expensive. This is where the difference approach for EIT offers an analytical workaround. In the difference setting, the same can be calculated by the volume integral of the dot product of electric fields, as given by [17]:

$$J_i^{mn\to pn}\big(\sigma(\boldsymbol{r})\big) = \frac{-1}{I}\int_{\Omega_i} E_{mn}\big(\sigma(\boldsymbol{r})\big)E_{pn}\big(\sigma(\boldsymbol{r})\big)d\Omega \tag{11}$$

In Eqn. (11), $E_{mn}\big(\sigma(\boldsymbol{r})\big)$ is the electric field across the sample in response to the conductivity distribution $\sigma(\boldsymbol{r})$, when a current *I* is applied across electrodes *m* and *n* (*n* being the sink). The integral is over the volume of the i^{th} cell.

The conductivity in the k^{th} iteration can then be updated based on the Jacobian and the difference between the reference and predicted voltage using the Newtown's method along with a regularization, as given by

$$\sigma_{k+1} = \sigma_k + (\boldsymbol{J}^T\boldsymbol{J} + \lambda\boldsymbol{I})^{-1}\boldsymbol{J}^T\big(\boldsymbol{V}_0 - \boldsymbol{V}_P(\sigma_k)\big), \tag{12}$$

where *I* is the identity matrix, and λ is the regularization coefficient.

A key limitation of the above reconstruction approach lies in the fact that the experimental measurement $\boldsymbol{V}_0$ for the sample of interest will include the impact of the contact resistances described earlier. The simulated response cannot include this because the contact resistances are unknown. To resolve this, consider making the same measurements on the virgin sample before deployment to get an initial base value for a sample with no defects. Then measure the sample during inspection. Assuming that the contact resistance before and after deployment remains constant, and the variance in the resistance at the electrode and wire contact (see Eqns. [4] to [6]) is small,

$$V_{mn}^{mn}|_{Initial}^{Expt} = IR_m^{Contact} + IR_{mn}^{Initial} + IR_n^{Contact} \tag{13}$$

$$V_{mn}^{mn}|_{Final}^{Expt} = IR_m^{Contact} + IR_{mn}^{Final} + IR_n^{Contact} \tag{14}$$

In the case of simulations, contact resistance is unknown and can be neglected to get

$$V_{mn}^{mn}|_{Initial}^{Sim} = IR_{mn}^{Initial} \tag{15}$$

$$V_{mn}^{mn}|_{Final}^{Sim} = IR_{mn}^{Final} \tag{16}$$

Whereas the initial value of R_{mn} can be simulated by assuming a defect free sample, the final value is unknown and can not be directly simulated. However, using Eqns. (13) to (16),

$$V_{mn}^{mn}|_{Final}^{Sim} = V_{mn}^{mn}|_{Initial}^{Sim} + V_{mn}^{mn}|_{Final}^{Expt} - V_{mn}^{mn}|_{Initial}^{Expt} \tag{17}$$

Thus, the following approximation can be made inside Eqn. (12):

$$\boldsymbol{V}_0 = \boldsymbol{V}_0|_{Initial}^{Sim} + \boldsymbol{V}_0|_{Final}^{Expt} - \boldsymbol{V}_0|_{Initial}^{Expt} \tag{18}$$

Note that Eqn. (12) is strictly valid only when the excited electrodes are the same as the measured electrodes. The validity and effectiveness of the approximation is evaluated in Section 4.

Last, a 12-electrode setup, as shown in Figure 17, was tested to improve the resolution of the defects. Note that the number of possible pair excitations increases as square of the number of electrodes.

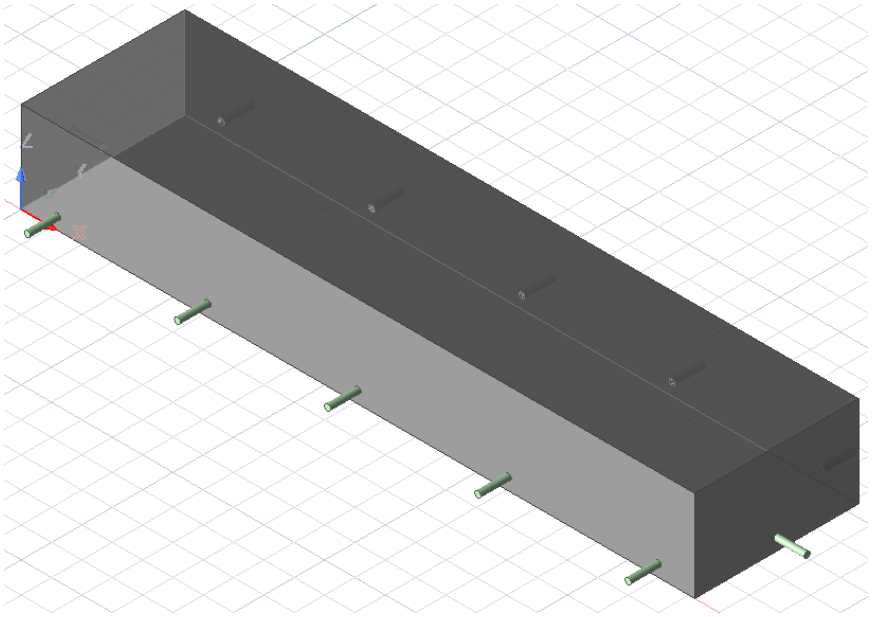

Figure 17. A 12-electrode setup for the rectangular block sample to improve the resolution of the reconstruction.

4. RESULTS

4.1 CRACK IMPACT: QUALITATIVE ANALYSIS

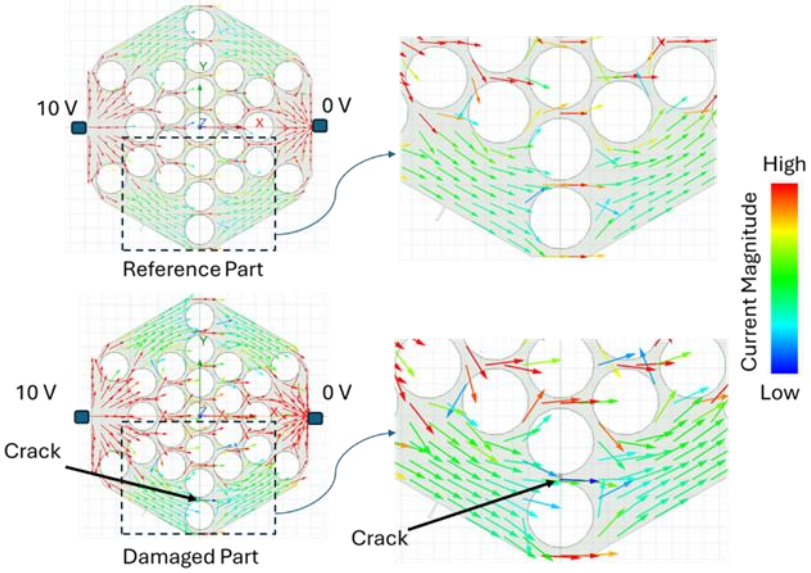

Figure 18. Variation in the current density across a slice of the full-scale hexagonal graphite block with and without a defect.

The primary objective of the present study is to test whether defects like cracks between walls in the graphite core have an impact on the current flow through the electrodes and whether it is significant enough to be discernable through impedance or voltage measurements. As a first test, the team evaluated the hexagonal graphite block sample (see Figure 12, left panel) with and without a crack in the wall between the two slots. Figure 18 shows the electric current density variation across the sample as a voltage is applied between electrodes at two opposite faces. The top panel shows a reference sample without any defects, whereas the bottom panel shows a sample with a crack between two slots. The current adopts an alternate path in the defect sample, shown by red arrows indicating high current density through paths above and below the region with defect. This is encouraging because it implies that such cracks may result in discernable changes in impedance, which may help detect and possibly localize such defects using the inverse model. The rest of this section probes this question in more detail.

4.2 ELECTRODE CONTACT IN RECTANGULAR BLOCK SAMPLE

Testing with spring-loaded pins resulted in visible mechanical wear on the graphite surface during placement and did not make solid, reliable contact. Measurement across the graphite sample with standard multimeter probes showed that resistance readings could swing heavily based on the contact angle and amount of pressure used. The repeatability of measurements was poor, with differences seen in excess of 100% in some cases. This finding pointed to further testing toward rigidly adhering electrodes to ensure repeatable, comparable readings rather than temporary mechanical coupling.

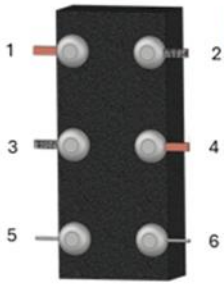

Electrode	Contact
1	Copper
2	Fabric
3	Fabric
4	Copper
5	Wire
6	Wire

Figure 19. Setup for measuring the impedance of the rectangular graphite block by attaching electrodes of different materials to the sample using silver epoxy.

Following this, the electrodes were attached at the top face of the sample using a silver epoxy as shown in Figure 19. Three different electrodes were tested, as described in Section 3.1: (1) copper tape, (2) conducting fabric, and (3) copper wire. The impedance was measured twice on the same day after recalibrating the apparatus, and the electrodes were disconnected from the measuring apparatus after every single measurement. The impedance values from this experiment are listed in Table 2. The total impedance values for the conducting fabric seem to be visibly higher than that of the other two electrodes. Thus, while it could be a viable candidate for use on other materials, considering graphite's low resistance values, the higher contact resistance seen in conducting fabric would likely be a cause for concern.

Table 2. Impedance values across electrode pairs in the rectangular graphite block for the setup shown in Figure 19.

Excitation Pair	Impedance Measurement ($m\Omega$)	
	1	2
(1,2)	125.39	161.6
(1,3)	146.14	168.59
(1,4)	53.117	54.748
(1,5)	63.801	56.864
(1,6)	54.085	53.979
(2,3)	246.37	290.51
(2,4)	153.93	180.48
(2,5)	162.97	180.95
(2,6)	152.37	178.89
(3,4)	163.48	187.46
(3,5)	171.08	189.61
(3,6)	163.95	186.34
(4,5)	79.959	78.369
(4,6)	68.427	73.909
(5,6)	77.546	74.159

Although the contact and the sample resistances (see Eqn. [3]) cannot be directly extracted from these measurements, if the sample is assumed to be defect-free, the symmetry of the sample can be used to deduce the approximate values of the two components. The following constraints can be applied using symmetries:

$$R_{12} = R_{56} = x_1 \tag{19}$$

$$R_{14} = R_{23} = R_{36} = R_{45} = x_2 \tag{20}$$

$$R_{15} = R_{26} = x_3 \tag{21}$$

$$R_{16} = R_{25} = x_4 \tag{22}$$

$$R_{13} = R_{24} = R_{35} = R_{46} = x_5 \tag{23}$$

$$R_{34} = x_6 \tag{24}$$

Table 3 lists the simulated values for each of these pairs, demonstrating that the symmetry constraints are satisfied in an ideal system.

Table 3. Simulated values of the impedance across each pair of electrodes indicating the symmetries shown in Eqns. (19) to (24) are satisfied.

Variable	Excitation Pair	Sample Resistance ($m\Omega$)
x_1	(1,2)	15.25
	(5,6)	15.26
x_2	(1,4)	16.36
	(4,5)	16.33
	(2,3)	16.34
	(3,6)	16.35
x_3	(1,5)	18.22
	(2,6)	18.16
x_4	(1,6)	18.19
	(2,5)	18.21
x_5	(1,3)	16.32
	(3,5)	16.33
	(2,4)	16.33
	(4.6)	16.33
x_6	(3,4)	14.90

Using these relations along with Eqn. (3), we can write:

$$AX = B \tag{25}$$

where:

$$A = \begin{pmatrix} 1 & 1 & 0 & 0 & 0 & 0 & 1 & 0 & 0 & 0 & 0 & 0 \\ 1 & 0 & 1 & 0 & 0 & 0 & 0 & 0 & 0 & 0 & 1 & 0 \\ 1 & 0 & 0 & 1 & 0 & 0 & 0 & 1 & 0 & 0 & 0 & 0 \\ 1 & 0 & 0 & 0 & 1 & 0 & 0 & 0 & 1 & 0 & 0 & 0 \\ 1 & 0 & 0 & 0 & 0 & 1 & 0 & 0 & 0 & 1 & 0 & 0 \\ 0 & 1 & 1 & 0 & 0 & 0 & 0 & 1 & 0 & 0 & 0 & 0 \\ 0 & 1 & 0 & 1 & 0 & 0 & 0 & 0 & 0 & 0 & 1 & 0 \\ 0 & 1 & 0 & 0 & 1 & 0 & 0 & 0 & 0 & 1 & 0 & 0 \\ 0 & 1 & 0 & 0 & 0 & 1 & 0 & 0 & 1 & 0 & 0 & 0 \\ 0 & 0 & 1 & 1 & 0 & 0 & 0 & 0 & 0 & 0 & 0 & 1 \\ 0 & 0 & 1 & 0 & 1 & 0 & 0 & 0 & 0 & 0 & 1 & 0 \\ 0 & 0 & 1 & 0 & 0 & 1 & 0 & 1 & 0 & 0 & 0 & 0 \\ 0 & 0 & 0 & 1 & 1 & 0 & 0 & 1 & 0 & 0 & 0 & 0 \\ 0 & 0 & 0 & 1 & 0 & 1 & 0 & 0 & 0 & 0 & 1 & 0 \\ 0 & 0 & 0 & 0 & 1 & 1 & 1 & 0 & 0 & 0 & 0 & 0 \end{pmatrix}; X = \begin{pmatrix} R_1^C \\ R_2^C \\ R_3^C \\ R_4^C \\ R_5^C \\ R_6^C \\ x_1 \\ x_2 \\ x_3 \\ x_4 \\ x_5 \\ x_6 \end{pmatrix}; B = \begin{pmatrix} R_{12}^{Total} \\ R_{13}^{Total} \\ R_{14}^{Total} \\ R_{15}^{Total} \\ R_{16}^{Total} \\ R_{23}^{Total} \\ R_{24}^{Total} \\ R_{25}^{Total} \\ R_{26}^{Total} \\ R_{34}^{Total} \\ R_{35}^{Total} \\ R_{36}^{Total} \\ R_{45}^{Total} \\ R_{46}^{Total} \\ R_{56}^{Total} \end{pmatrix} \quad (26)$$

Thus, X can be calculated using the pseudo inverse of A as:

$$X = pseudoinverse(A) \times B \quad (27)$$

Using Eqn. (27), the contact resistance was calculated on the six electrodes, which are listed in Table 4. As noted earlier, the conducting fabric (electrodes 2 and 3) exhibits the highest contact resistance, whereas both copper tape and copper wire show reasonably smaller values that are consistent across the two runs. Using the average across these two, the sample resistances across each electrode pair are obtained, as listed in Table 5. Notably, the experimental resistance values are higher than the simulated values, though in the similar order of magnitude. On average, the simulation estimates are about 0.62 times smaller than those of the experiments. This may be a result of a lower bulk conductivity in the actual sample compared with that used in the simulations. Further, the ratio between the simulated and experimental estimates for each independent symmetric value from Eqns. (19) to (24) vary between 0.37 and 0.84. Although this may suggest that the actual sample does not exhibit the same scaling between the symmetric estimates as compared to the simulations, this could also be a result of calculating experimental values while neglecting variations caused by contact between the electrodes and the wire. This could be significant. Also, fabric contact exhibits noticeably higher contact resistance, potentially distorting estimates for sample resistances, which are an order of magnitude smaller. Thus, further analysis is needed with all electrodes using either copper wire or copper tape electrodes. Copper tape shows lower contact resistance, but it presents challenges with repeatability due to physical deformation of the copper foil after repeated disconnections and reconnections of the alligator clamps used to connect to the potentiostat, resulting in inconsistent readings across test runs. The wire electrodes exhibited slightly higher contact resistance than that of the copper tape but were far superior in terms of repeatability of measurements. Based on these findings, epoxied wire electrodes were used in all testing going forward.

Table 4. Contact resistances for the rectangular block calculated using Eqn. (25).

Variable	Contact Material	Contact Resistance ($m\Omega$)		
		Measurement (B)		
		1	2	Mean
R_1^C	Copper	6.71	7.34	7.03
R_2^C	Fabric	106.34	131.50	118.92
R_3^C	Fabric	110.41	128.99	119.70
R_4^C	Copper	17.38	17.10	17.24
R_5^C	Wire	34.92	28.38	31.65
R_6^C	Wire	25.17	25.22	25.19

Table 5. Sample resistances for the rectangular block calculated using Eqn. (25), compared to simulated estimates for the same.

Variable	Sample Resistance ($m\Omega$)				Ratio (Sim/Expt)
	Measurement (B)			Simulations	
	1	2	Mean		
x_1	14.90	21.66	18.28	15.25	0.83
x_2	28.67	31.34	30.01	16.36	0.55
x_3	21.52	21.66	21.59	18.22	0.84
x_4	21.96	21.24	21.60	18.19	0.84
x_5	27.72	31.99	29.86	16.32	0.55
x_6	35.70	41.38	38.54	14.9	0.37
Mean	25.08	28.21	26.64	16.54	0.62

4.3 HEXAGONAL BLOCK WITH COPPER WIRE ELECTRODES

Next, the hexagonal block sample was tested (see Figure 12) using copper wire electrodes attached to the top face using silver epoxy. Again, symmetry considerations can be used to obtain three independent resistance values associated with sample:

$$R_{12} = R_{23} = R_{34} = R_{45} = R_{56} = R_{16} = x_1 \tag{28}$$

$$R_{13} = R_{24} = R_{35} = R_{46} = R_{15} = R_{26} = x_2 \tag{29}$$

$$R_{14} = R_{25} = R_{36} = x_3 \tag{30}$$

As before, using Eqns. (28) to (30) along with Eqn. (3) gives:

$$AX = B \tag{31}$$

where:

$$A = \begin{pmatrix} 1 & 1 & 0 & 0 & 0 & 0 & 1 & 0 & 0 \\ 1 & 0 & 1 & 0 & 0 & 0 & 0 & 1 & 0 \\ 1 & 0 & 0 & 1 & 0 & 0 & 0 & 0 & 1 \\ 1 & 0 & 0 & 0 & 1 & 0 & 0 & 1 & 0 \\ 1 & 0 & 0 & 0 & 0 & 1 & 1 & 0 & 0 \\ 0 & 1 & 1 & 0 & 0 & 0 & 1 & 0 & 0 \\ 0 & 1 & 0 & 1 & 0 & 0 & 0 & 1 & 0 \\ 0 & 1 & 0 & 0 & 1 & 0 & 0 & 0 & 1 \\ 0 & 1 & 0 & 0 & 0 & 1 & 0 & 1 & 0 \\ 0 & 0 & 1 & 1 & 0 & 0 & 1 & 0 & 0 \\ 0 & 0 & 1 & 0 & 1 & 0 & 0 & 1 & 0 \\ 0 & 0 & 1 & 0 & 0 & 1 & 0 & 0 & 1 \\ 0 & 0 & 0 & 1 & 1 & 0 & 1 & 0 & 0 \\ 0 & 0 & 0 & 1 & 0 & 1 & 0 & 1 & 0 \\ 0 & 0 & 0 & 0 & 1 & 1 & 1 & 0 & 0 \end{pmatrix}; X = \begin{pmatrix} R_1^C \\ R_2^C \\ R_3^C \\ R_4^C \\ R_5^C \\ R_6^C \\ x_1 \\ x_2 \\ x_3 \end{pmatrix}; B = \begin{pmatrix} R_{12}^{Total} \\ R_{13}^{Total} \\ R_{14}^{Total} \\ R_{15}^{Total} \\ R_{16}^{Total} \\ R_{23}^{Total} \\ R_{24}^{Total} \\ R_{25}^{Total} \\ R_{26}^{Total} \\ R_{34}^{Total} \\ R_{35}^{Total} \\ R_{36}^{Total} \\ R_{45}^{Total} \\ R_{46}^{Total} \\ R_{56}^{Total} \end{pmatrix} \quad (32)$$

Table 6 lists the impedance measurements across each excitation pair, which represents R^{Total} in Eqn. (3). These values constitute matrix B in Eqn. (32). Using these and the pseudo inverse of A as before, the contact resistances are obtained for each electrode and are listed in Table 7. Note that the impedance value across electrodes 3 and 4 is significantly higher than that of all other electrode pairs. If this was caused by a high contact resistance at either of those electrodes, then the higher values would have also shown up in other measurements for that electrode. Thus, this is a result of either a defect in the sample between these electrodes or an error during measurement. In either case, removing this measurement will likely give a better estimate of the contact and sample resistances using the pseudo inverse method.

Table 6. Impedance measurement across each electrode pair (i.e., *R* total from Eqn. [3]). The value for excitation (3, 4) is an outlier and is marked in red.

Excitation Pair	Impedance Measurement ($m\Omega$)
(1,2)	106.24
(1,3)	109.12
(1,4)	111.56
(1,5)	108.20
(1,6)	107.65
(2,3)	106.13
(2,4)	114.83
(2,5)	109.09
(2,6)	110.42
(3,4)	126.33
(3,5)	111.10
(3,6)	116.27
(4,5)	105.83
(4,6)	110.17
(5,6)	105.53

Table 7 lists the contact resistances using the whole data, as well as when the (3,4) measurement was removed. All contacts show similar resistance values, with a mean and standard deviation of 36.63 and 1.22 mΩ, respectively. Note that the 1.22 mΩ contains the standard deviation from both the sample–electrode contact and the electrode–wire contact, the latter probably being the smaller one (see Eqn. [4]). Thus, the standard deviation from just the electrode–wire contact is probably of a lower magnitude. This justifies the assumption in the previous calculations that the variations due to electrode–wire contact are small compared to the contact resistance and can be neglected during the calculations.

Table 7. Contact resistances calculated using Eqns. (28) to (32).

Variable	Contact Resistance ($m\Omega$)	
	Whole Data	(3,4) removed
R_1^C	34.44	35.57
R_2^C	35.42	36.55
R_3^C	40.98	37.76
R_4^C	40.93	37.70
R_5^C	33.68	34.81
R_6^C	36.26	37.38
Mean	36.95	36.63
STD	3.22	1.22

Table 8. Sample resistances from simulations and those calculated using Eqns. (28) to (32) after removing the excitation pair (3, 4).

Variable	Sample Resistance ($m\Omega$)		x/x_1		Ratio (Sim/Expt)
	Experiment	Simulation	Experiment	Simulation	
x_1	33.46	19.72	1.0	1.0	0.59
x_2	37.38	22.09	1.12	1.12	0.59
x_3	39.05	22.80	1.17	1.16	0.58

Next, the three sample resistances from Eqns. (28) to (32), as shown in Table 8, along with the simulated values for the same. As before, the experimental values are higher than the simulated values. Interestingly, the ratios x_2/x_1 and x_3/x_1 match well between the simulations and the experiments. This indicates that the resistances across electrode pairs show the same scaling for both simulations and experiments. Thus, the ratio between simulation and experimental estimates is constant at 0.59, which is close to the average value of this ratio in the rectangular sample (0.62). As discussed earlier in this section, this ratio is most likely indicative of a difference between the bulk conductivity in the simulations compared with that of the experiments. Following this, the bulk value of the conductivity for the sample in simulations was scaled down by a factor of 0.59. Table 9 shows the sample resistances from the simulations after performing this scaling. The simulations were performed with and without the contact resistances obtained from Table 7 (see Figure 13. Approach for contact resistance. (left) Electrodes modeled as thin cylinders: the first two parts shown in green are modeled with brass, and the conductivity of the third part shown in brown is controlled to model the contact resistance variations. (right) The resistance between electrodes 1 and 3 is approximated as the sum of sample resistance and contact resistance.). In both setups, scaling the bulk conductivity leads to excellent agreement between the simulations and experiments. The total impedance between each electrode pair from the simulations, after

inclusion of the contact resistances, are shown in Table 10. Again, the simulation estimates are in good agreement with the experiments, indicating that the simulations can be used to model both the sample and contact resistances.

Table 9. Sample resistances from simulations after scaling the bulk conductivity by 0.59, compared against those calculated using Eqns. (28) to (32) after removing the excitation pair (3, 4).

Variable	Sample Resistance ($m\Omega$)			Ratio (Sim/Expt)	
	Experiment	Simulation		Without Contact Resistance	With Contact Resistance
		Without Contact Resistance	With Contact Resistance		
x_1	33.46	33.38	34.08	1.00	1.02
x_2	37.38	37.41	38.10	1.00	1.02
x_3	39.05	38.62	39.30	0.99	1.01

Table 10. Total impedance across each electrode pair from experiments and computed using simulations with scaled bulk conductivity and inclusion of contact resistance.

Excitation Pair	Impedance Measurement ($m\Omega$)		Sim/Expt
	Experiments	Simulation	
(1,2)	106.24	107.28	1.01
(1,3)	109.12	112.55	1.03
(1,4)	111.56	113.65	1.02
(1,5)	108.20	109.47	1.01
(1,6)	107.65	108.06	1.00
(2,3)	106.13	109.52	1.03
(2,4)	114.83	113.50	0.99
(2,5)	109.09	111.72	1.02
(2,6)	110.42	113.01	1.02
(3,4)	126.33	110.67	0.88
(3,5)	111.10	111.70	1.01
(3,6)	116.27	115.50	0.99
(4,5)	105.83	107.74	1.02
(4,6)	110.17	114.30	1.04
(5,6)	105.53	107.17	1.02

4.4 DEFECT IMPACT AND RECONSTRUCTION

Next, the scaled value of the bulk conductivity, along with the contact resistances obtained from the previous subsection, were used to analyze the impact of defects on the measured impedance values. Table 11 shows the change in total impedance across each electrode about the reference value caused by the introduction of defects into the sample. Three cases are considered: (1) a single crack in the rectangular sample, (2) two cracks in the rectangular sample, and (3) a crack between two slots in the hexagonal sample (see Figure 14). Evidently, the impedance change is high for the electrode pairs that surround the defect. For example, the crack is between electrodes 5 and 6 in the hexagonal sample and leads to an

impedance change of 3.38 mΩ. Table 11 shows the maximum change for each case in bold. The rectangular sample shows smaller changes, especially for a single crack. This could be due to the specific location of the crack between two slots in the hexagonal sample. Other locations may not be as sensitive. The important point is that, at least for some cracks, the change is a few times greater than the overall estimated standard deviation (approximately 1.2 mΩ) in the contact resistance (see Table 7). Considering that the electrode–wire contact will have a smaller deviation than 1.2 mΩ , it should be possible to make multiple measurements to reduce the noise and resolve impedance changes caused by defects like the one tested here.

Table 11. Change in impedance between the reference and defect sample, computed using simulations with scaled bulk conductivity and inclusion of contact resistances.

Excitation Pair	Change in Impedance (*m*Ω)		
	Hexagonal Block with 1 Crack	Rectangular Block	
		1 Crack	2 Cracks
(1,2)	0.17	-0.01	0.00
(1,3)	0.31	0.80	0.82
(1,4)	0.73	0.67	0.74
(1,5)	1.80	0.76	**1.76**
(1,6)	0.34	0.73	1.33
(2,3)	0.07	**0.87**	0.87
(2,4)	0.28	0.66	0.63
(2,5)	1.14	0.73	1.70
(2,6)	0.60	0.79	1.30
(3,4)	0.09	0.02	0.02
(3,5)	0.62	0.05	1.00
(3,6)	1.10	0.02	0.51
(4,5)	0.25	0.00	0.92
(4,6)	1.83	0.05	0.61
(5,6)	**3.38**	-0.06	0.14

The sensitivity of the measurements to the location of the crack was tested by moving the crack along the length of the sample. Figure 20 shows the variation in measurements across four key electrode pairs that capture the crack. Note that these simulations were performed before scaling the bulk conductivity and inclusion of contact resistances. Thus, the values have been presented as percentage changes about the reference sample. The values vary between 3.5% and 1.8%, and these preliminary results show some pattern and sensitivity (though small) to the location of the sample. Although these patterns may encode information necessary to localize the defects, further tests are necessary for more conclusive evidence.

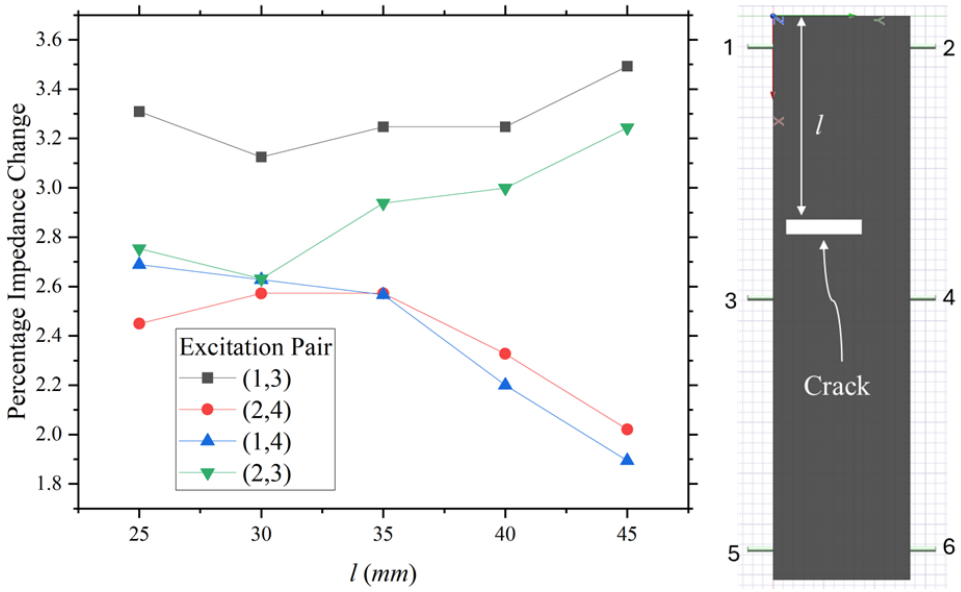

Figure 20. Variation in voltage measurements across key pairs of electrodes as a crack is moved along the length of the sample.

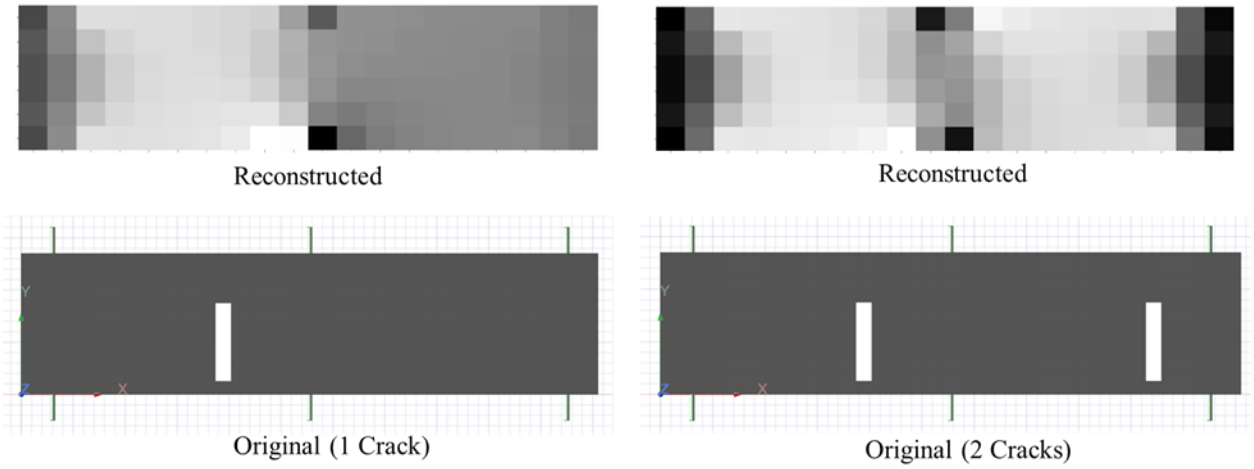

Figure 21. Reconstruction of one and two cracks in the rectangular sample after six iterations.

Figure 21 shows the reconstruction of samples with one and two cracks after six iterations. The high conductivity pixels are shown in black (graphite), and low conductivity pixels (defect) are shown in white. The inverse model is able to detect the presence of a crack and its location on the right or left of the sample. The overall reconstruction is blurry, but this is expected when using only a six-electrode setup. Better localization can be achieved by using more electrodes (discussed in Section 4.6). Note that these reconstructions were performed without scaling the bulk conductivity and inclusion of contact resistances in the simulations. The impact of these effects is discussed in the next subsection. Figure 22 shows the variation of the root mean square (RMS) value of the difference between the reference and the predicted voltage measurements with the reconstruction iterations (see Eqn. [13]). The black curve used the perturbation approach for calculating the Jacobian. This is computationally expensive, and thus a lower resolution was used (10×4), and the Jacobian was calculated only once during the first iteration. The red curve uses the same resolution but with the analytical Jacobian from Eqn. (12), updated every iteration. The use of the analytical Jacobian not only results in significant time savings but also produces lower

error values. The blue curve shows the same with a higher resolution, indicating that the system can converge to lower error values using more iterations for higher resolutions. The green curve shows the results for two crack systems and seems to be converging toward similar values. More tests are needed to establish if there is a lower bound to error values at which the reconstruction stops improving with more iterations. The magnitude of the regularization parameter λ will also play a role in this convergence.

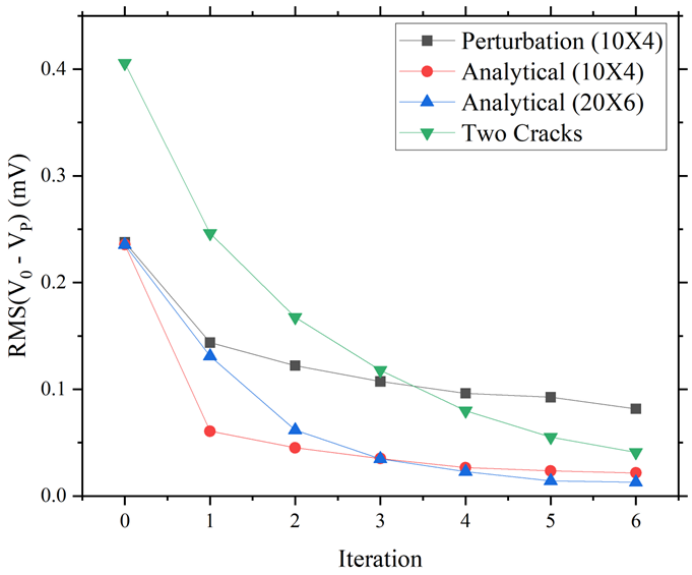

Figure 22. Variation in the difference between the reference and predicted voltage response across reconstruction iterations for different resolutions and Jacobian approaches.

4.5 HANDLING UNKNOWN CONTACT RESISTANCE

As discussed earlier, a real sample will contain unknown contact resistances, which cannot directly be included in the simulations informing the reconstruction algorithm. One approach to resolve this is to use the virgin sample, without defects, along with symmetry constraints like the one used here to get an approximate estimate of the contact resistances. Note that these symmetries may not always be present or may not be enough to calculate contact resistance. However, as demonstrated in Eqn. (19), the reconstruction can still be performed as long as the reference values of the voltages are available from the virgin sample. The contact resistance model for the electrode was used to simulate and test this condition. Two sets of simulations were performed on the virgin and defect samples. The first set was performed without the inclusion of contact resistance, and the second set included contact resistance, serving as a surrogate for experimental data. Figure 23 shows the comparison of the difference between the voltage measurements (total 75 measurements) from the virgin and defect samples, with and without the inclusion contact resistances. The two estimates are close for most measurements but show some deviation for a few cases. Note that Eqn. (19) was derived only for cases in which the excited electrode pair was the same as the measured electrode pair (15 measurements out of 75). Figure 24 specifically covers these measurements for each pair excitation. The agreement between the two cases is better for these measurements, but there is still some deviation for a few data points, like the excitation pair (1, 5). Thus, Eqn. (19) may not be strictly valid, which can have an impact on the final reconstruction. To test this impact, reconstruction was performed on data with and without the inclusion of contact resistance, and the comparison between the two is shown in Figure 25. Whereas the algorithm is still able to detect and localize the defect to an extent even after the inclusion of contact resistances, the reconstruction gets slightly distorted. Thus, it may be possible to detect defects in the presence of unknown contact

resistances, but the localization capabilities are likely to be limited. The incorporation of more electrodes may alleviate this problem.

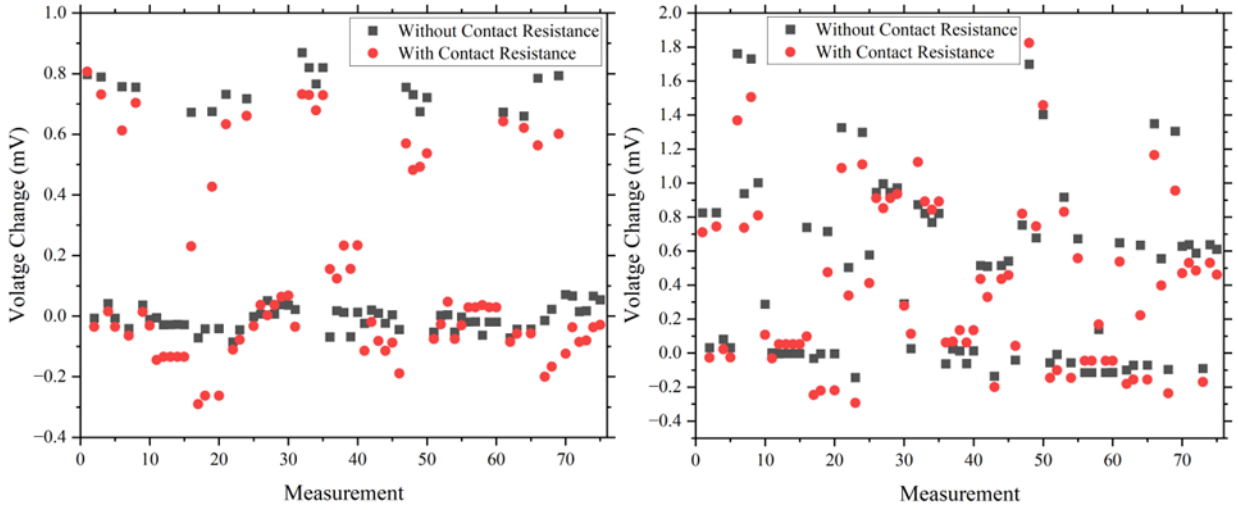

Figure 23. Difference between the reference and defect sample voltage response with and without inclusion of contact resistance for (left) a single crack and (right) two cracks.

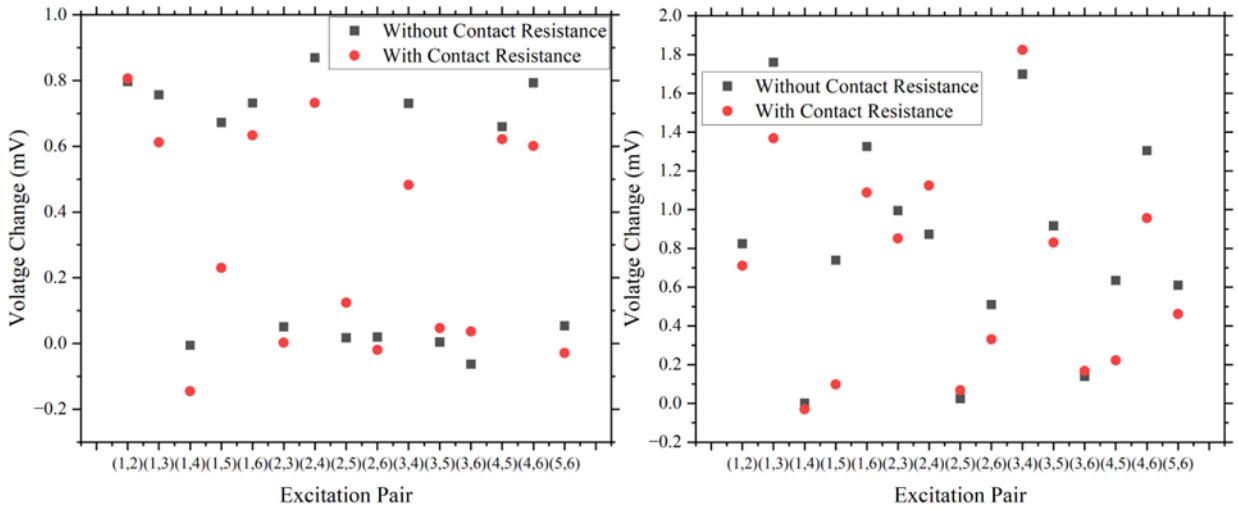

Figure 24. Difference between the reference and defect sample voltage when the excited pair is the measured pair, with and without inclusion of contact resistance, for (left) a single crack and (right) two cracks.

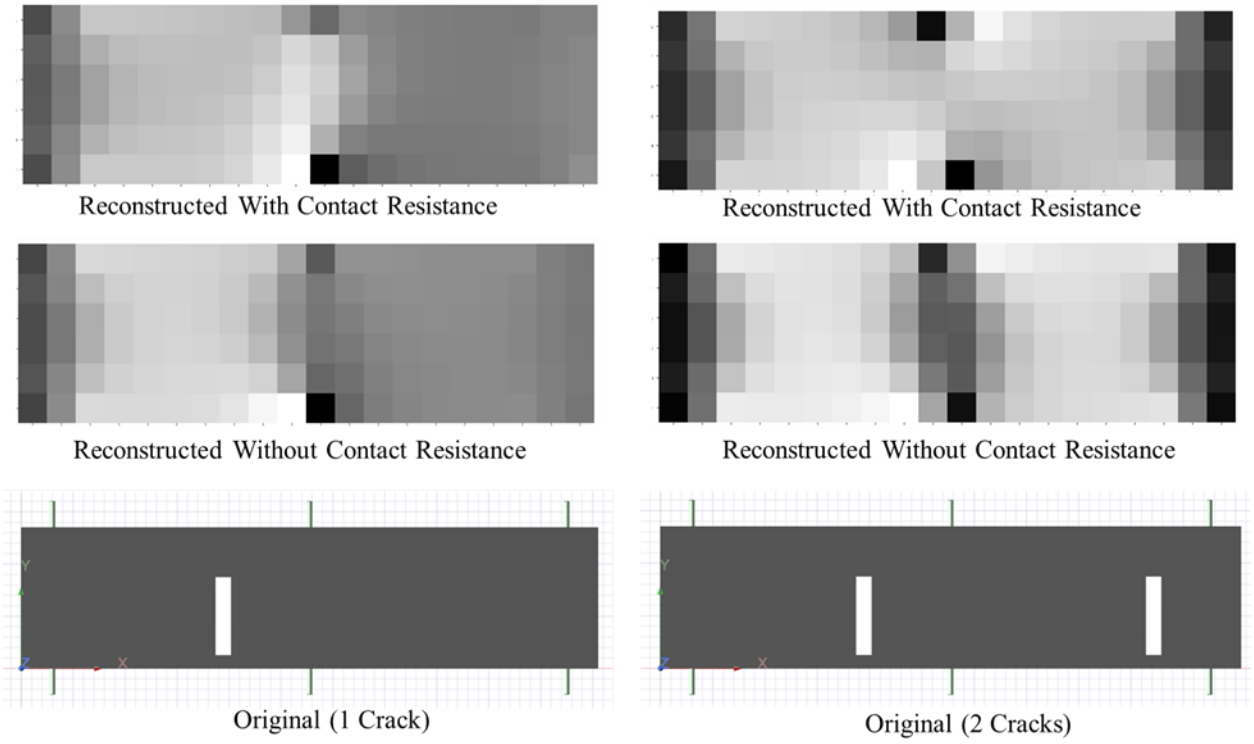

Figure 25. Comparison of the reconstruction after five iterations, using measurements with and without contact resistance.

4.6 HIGHER RESOLUTION WITH MORE ELECTRODES

Figure 26 shows the reconstruction after 5 iterations using the 12-electrode setup from Figure 17. Essentially, the setup contains five electrodes along each length, with one electrode each on the front and back face. Note that these reconstructions were performed with the initial value of the bulk conductivity (no 0.59 scaling) and without any contact electrodes. While the six-electrode setup was only able to detect whether there was a crack in the left or right half of the sample, the 12-electrode setup was able to detect in which quarter the crack was present. Though not explicitly tested here, for smaller cracks, this setup should also be able to resolve if the crack is on the top or bottom half.

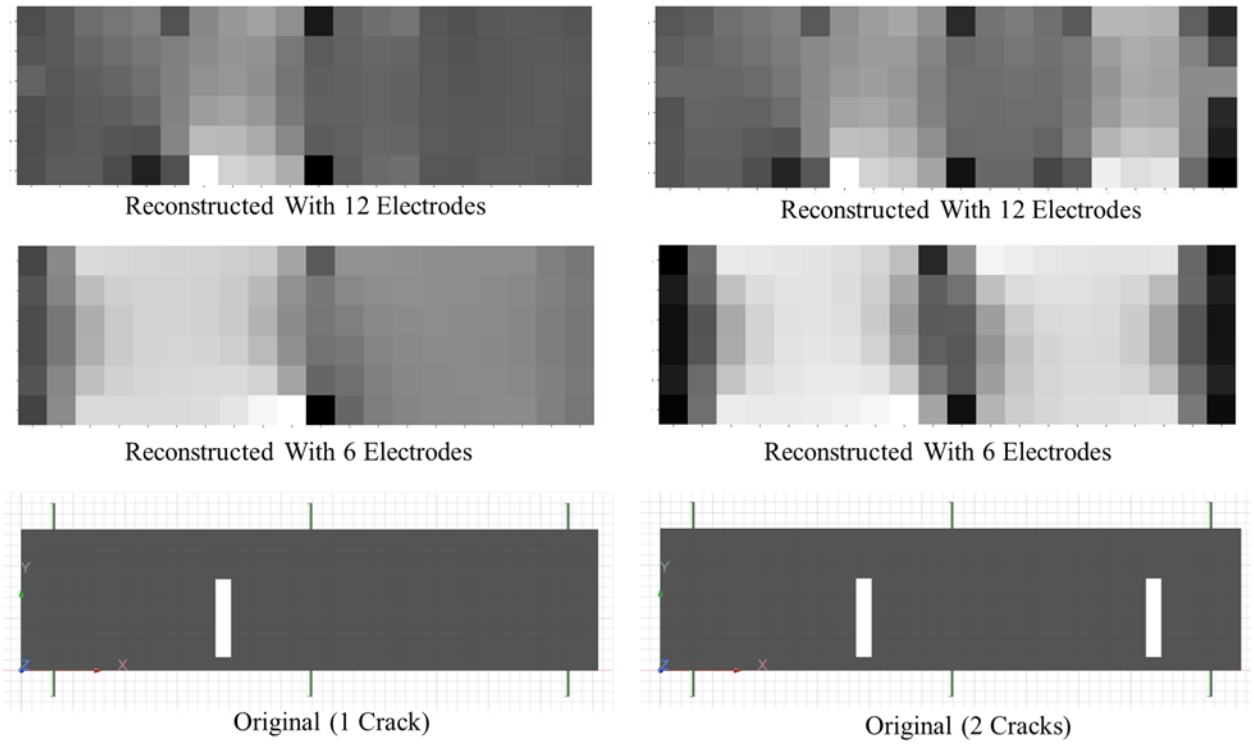

Figure 26. Comparison of reconstruction after 5 iterations using 6 vs. 12 electrodes.

5. DISCUSSION

5.1 MODELING VS. EXPERIMENTAL DISCREPANCIES

As seen in Sections 4.2 and 4.3, the two major sources of discrepancies between the experiments and the simulations arise from the contact resistance and the mismatch between the bulk conductivity of the real vs. simulated sample. The use of copper wire electrodes attached to the sample using silver epoxy resolved the contact resistance issue to a large extent. With this setup, symmetry constraints were used to compute an approximate estimate of the contact resistance and the ratio between the simulated and real bulk conductivity of the sample. Although this ratio may not capture all the discrepancies, it was likely responsible for most of them. Incorporating this scaling of the bulk conductivity, along with the contact resistances, led to excellent agreement between the simulated and experimental impedance measurements. However, more testing is required, especially with defect samples, to establish if this approach is complete or if other factors are missing from the model.

5.2 IMPLICATIONS FOR RESOLVABLE DEFECTS

Although experimental data on defect samples are not available yet, the simulations indicate that the hexagonal sample representative of the microreactor component can result in about 3.8 mΩ of impedance change across key electrodes due to a through crack along a wall joining two slots. The standard deviation in the contact resistance estimates was computed to be approximately 1.2 mΩ. This includes resistance at both the sample–electrode contact and the electrode–wire contact. The former may not be a cause of concern, as long as it remains constant between the reference and defect samples (though it may result in some distortion), whereas the latter is likely to be of a smaller magnitude. Further, the latter can be

minimized by making multiple measurements (goes down as $1/\sqrt{N}$ for N measurement). In the rectangular samples, the reconstruction algorithm was able to detect defects that resulted in smaller impedance changes. Thus, there is a strong chance of resolving such defects in the hexagonal sample. However, conclusive statements can only be made once the reconstruction is performed on experimental data from the defect samples.

5.3 EXPECTED SPATIAL RESOLUTION

The resolution of the defect is largely dependent on the number of electrodes. For the six-electrode setup with three electrodes on each side, the model was able to resolve which half of the sample contained the crack. When the electrodes were increased to 12, the model resolved the crack's location to the quarter of the sample (i.e., a region of approximately 27 mm). The actual resolution in the sample of interest would depend on the sample size and the number of electrodes. Note that although in principle, higher resolution can be obtained by increasing the number of electrodes, there are practical limitations, as the number of excitation pairs increase as square of the number of electrodes. However, some of this load can be alleviated by leveraging ML for better sample placement and selective pair excitations.

5.4 REMAINING GAPS AND SUGGESTED FUTURE WORK

As observed from the present study, the key challenge of using EIT on graphite is attaching electrodes to the sample with minimal contact resistance and high enough repeatability. The electrical property measurement of the hexagonal block shows promise for EIT measurement with a multiplexing setup. With a multiplexer mitigating contact resistance variance, the low overall resistance between epoxied wire electrodes is expected to allow physical defects to be located and resolved when introduced into future samples. The modeling results further bolster this expectation.

The reconstruction resolution was found to be highly dependent on the number of electrodes. However, as the number of pair excitations increases as the square of the number of electrodes, more efficient strategies can be adopted for electrode placement and selective pair excitation for maximizing information extraction using ML techniques. ML can also be used for developing surrogate models for the forward problem to accelerate the reconstruction algorithm and perform more iterations. Further, ML can be employed for a smarter approach to selecting the regularization parameter. In particular, an adaptive regularization approach can enable converging to lower error bounds at higher iteration steps.

6. SUMMARY AND CONCLUSIONS

This feasibility assessment demonstrates the potential for using EIT to detect and localize structural defects that may arise in graphite components used in microreactors. Experimental testing identified an electrode material and adhesion method that can be used in a lab setting to minimize contact resistance variability in order to perform future testing to validate results seen from the modeled simulations of defects. These simulations validated the necessary sensitivity of this measurement method for graphite components, showing that through-wall defects in a representative hexagonal graphite block resulted in impedance deviations measurably larger than deviations in contact resistance. Simulations of a twelve-electrode configuration demonstrated notable improvements in spatial resolution compared with that of models of the tested six-electrode samples. This improved spatial resolution allows for defect localization within a tighter window in comparison with the coarser results seen in the six-electrode sample.

Although challenges such as handling contact resistance variation and improving defect construction remain, the findings in this report provide a robust foundation for future work. Implementing multiplexing and optimizing electrode arrays will enhance the measurement repeatability and accuracy of

defect localization. These improvements have the potential to establish a route forward for validation that EIT can be a robust method for in situ structural health monitoring of graphite components, ensuring microreactor safety and longevity.

7. REFERENCES

[1] R. Testoni, A. Bersano, S. Segantin, Review of nuclear microreactors: Status, potentialities and challenges, Prog. Nucl. Energy 138 (2021) 103822.

[2] D.E. Shropshire, G. Black, K. Araújo, Global market analysis of microreactors, Idaho National Lab.(INL), Idaho Falls, ID (United States), (2021).

[3] G. Black, D. Shropshire, K. Araújo, A. van Heek, Prospects for Nuclear Microreactors: A Review of the Technology, Economics, and Regulatory Considerations, Nucl. Technol. 209(sup1) (2023) S1-S20.

[4] P. Ramuhalli, S.M. Cetiner, Concepts for Autonomous Operation of Microreactors, ORNL/TM-2019/1305, Oak Ridge National Laboratory, Oak Ridge, TN (2019).

[5] W. Williams, P. Ramuhalli, I. Greenquist, Development of microreactor automated control system (macs): surrogate plant-level modeling and control algorithms integration, Oak Ridge National Laboratory (ORNL), Oak Ridge, TN (United States), (2023).

[6] J.A. Farber, A.Y. Al Rashdan, M.E. Montezzo Coelho, Creating a Simulation Platform for Research and Development of Advanced Control Methods, Idaho National Laboratory (INL), Idaho Falls, ID (United States), (2023).

[7] F. Aldebie, K. Fernandez-Cosials, Y. Hassan, Neutronic and thermal analysis of heat pipe cooled graphite moderated micro reactor, Nucl. Eng. Des. 413 (2023) 112483.

[8] F. Aldebie, K. Fernandez-Cosials, Y. Hassan, Thermal-mechanical safety analysis of heat pipe micro reactor, Nucl. Eng. Des. 420 (2024) 113003.

[9] B.J. Marsden, M. Haverty, W. Bodel, G.N. Hall, A.N. Jones, P.M. Mummery, M. Treifi, Dimensional change, irradiation creep and thermal/mechanical property changes in nuclear graphite, International Materials Reviews 61(3) (2016) 155-182.

[10] T.D. Burchell, Radiation Effects in Graphite and Carbon-Based Materials, MRS Bulletin 22(4) (1997) 29-35.

[11] Poco Graphite, Inc. (2005, July 21). *Graphite materials – AXF-5Q*. Retrieved from http://www.poco.com/us/Graphite/axf.asp

[12] Keysight Technologies. (n.d.). E4990A Impedance Analyzer, 20 Hz to 10/20/30/50/120 MHz. Retrieved August 14, 2025, from https://www.keysight.com/...

[13] Dimas, Christos, Vassilis Alimisis, Nikolaos Uzunoglu, and Paul P. Sotiriadis, Advances in electrical impedance tomography inverse problem solution methods: From traditional regularization to deep learning, IEEE Access 12 (2024): 47797-47829.

[14] Colibazzi, Francesco, Damiana Lazzaro, Serena Morigi, and Andrea Samoré, Learning nonlinear electrical impedance tomography, Journal of Scientific Computing 90, no. 1 (2022): 58.

[15] Ansys Maxwell, Release 2024 R2, ANSYS, Inc.

[16] Liu, Benyuan, Bin Yang, Canhua Xu, Junying Xia, Meng Dai, Zhenyu Ji, Fusheng You, Xiuzhen Dong, Xuetao Shi, and Feng Fu, pyEIT: A python based framework for Electrical Impedance Tomography, SoftwareX 7 (2018): 304-308.

[17] Brandstatter, Bernhard. "Jacobian calculation for electrical impedance tomography based on the reciprocity principle." *IEEE transactions on magnetics* 39, no. 3 (2003): 1309-1312.